

Available online at www.sciencedirect.com

jmr&t
Journal of Materials Research and Technology
journal homepage: www.elsevier.com/locate/jmrt



Simulation of residual stress and micro-plastic deformation induced by laser shock imprinting on TC4 titanium alloy aero-engine blade

Mengyue Wang, Xizhang Chen*, Fengze Dai, Kang Peng, Ramachandra Arvind Singh, Sergey Konovalov

School of Mechanical and Electrical Engineering, Wenzhou University, Wenzhou 325035, PR China

ARTICLE INFO

Article history:

Received 9 August 2023

Accepted 21 September 2023

Available online 26 September 2023

Keywords:

Laser shock imprinting
Surface morphology control
Finite element analysis
Residual stress
Plastic deformation

ABSTRACT

In laser shock processing (LSP) of aero-engine blades, overlap marks due to spot overlapping cause irregular surface morphology that becomes a source of cracks under fatigue behaviors. This reduces the beneficial effect of compressive residual stress induced by LSP and undermines fatigue performance of blades. In this paper, laser shock imprinting (LSI) is proposed to improve fatigue performance of aero-engine blades. In this process, a layer of contact film with micro-grooves is placed between the absorption layer and the workpiece (blade) of the LSP. By using the double action of laser shock wave and micro-grooves in contact film, blade surface morphology is transformed towards the direction conducive to improve its fatigue performance. Using ABAQUS software, Johnson-Cook model and Fabbro model were considered to study the plastic rheological behavior of blade surface material induced by LSI. Effect of process parameters namely, peak pressure, impact number and spot overlapping ratio on residual stress and micro-plastic deformation of blade surface were studied. Simulation results showed that under the action of laser shock wave, blade surface material flowed into micro-grooves in contact film via extrusion plastic deformation. This resulted in micro-bulge morphology having geometrically specific arrangement on blade surface, which achieved accurate control of micro-plastic deformation on blade surface. Increase in peak pressure and impact number increase the surface micro-bulges height. However, increase in peak pressure lowers the stress difference between bulging edge and non-bulge zones. It was found that 33% spot overlapping impact resulted in more uniform surface micro-bulge morphology on blade surface.

© 2023 The Author(s). Published by Elsevier B.V. This is an open access article under the CC BY-NC-ND license (<http://creativecommons.org/licenses/by-nc-nd/4.0/>).

1. Introduction

Blade is the key component of an aero-engine. Blades operate in harsh working environments (i.e. high temperature, high pressure and high speed for long duration of time), and so

experience fatigue damage [1–4]. This seriously affects the safety and reliability of aero-engines. Performance of aero-engine depends on material and manufacturing technology of blades [5]. TC4 titanium alloy (alloy composition Ti-6Al-4V) is an $\alpha+\beta$ type dual-phase titanium alloy that is widely used in

* Corresponding author.

E-mail address: chenxizhang@wzu.edu.cn (X. Chen).

<https://doi.org/10.1016/j.jmrt.2023.09.225>

2238-7854/© 2023 The Author(s). Published by Elsevier B.V. This is an open access article under the CC BY-NC-ND license (<http://creativecommons.org/licenses/by-nc-nd/4.0/>).

aerospace applications due to its excellent mechanical properties at high temperatures [6–8].

Fatigue performance of blade is closely related to its surface integrity [9,10] (i.e. micro-morphology, roughness, residual stress and micro-hardness, etc.), and so it is important to strengthen surface of aero-engine blade to extend its service life. Laser shock processing/peening (LSP) [11,12] is an advanced surface-strengthening technology that uses short pulse and high-power laser to induce high-pressure plasma shock waves on surface of metallic materials to improve their fatigue performance. From the mid-1990s to the beginning of the 21st century, LSP technology has been successfully applied to the production and maintenance of engine blades such as those in F101, F110, F414 and F119 in United States, which has substantially improved fatigue life of blades [13]. However, in conventional LSP due to overlapping of laser spots, blade surface becomes irregular in its morphology (depression and flange interlacing) that becomes a source of cracks under fatigue behaviors, and also reduces the beneficial effect of compressive residual stress induced by laser shock [14,15]. Therefore, it is of great significance to effectively control morphology of blade surface in laser shock in order to make it develop in a direction conducive to the improvement of blade fatigue performance for LSP of aero-engine blades.

In this paper, laser shock imprinting (LSI) technology is proposed to effectively control blade surface morphology. In contrast to conventional LSP, in LSI a high strength, high hardness and high elasticity metal film (contact film) is placed in between the absorption layer and the workpiece. One surface of contact film has etched micro-grooves with specific geometrical dimension and distribution. The micro-grooved surface of contact film is placed on the workpiece. This arrangement in LSI is schematically shown in Fig. 1. When a high-power density pulsed laser beam is emitted, it gets transmitted by the focusing lens and passes through the constraint layer to reach the absorption layer that absorbs laser energy and generates high-pressure plasma. The plasma continues to heat up and explodes, inducing a super-pressure shock wave that impinges on contact film. Pressure induced by the laser shock promotes the mutual extrusion between the contact film and the workpiece, thereby it forms micro-

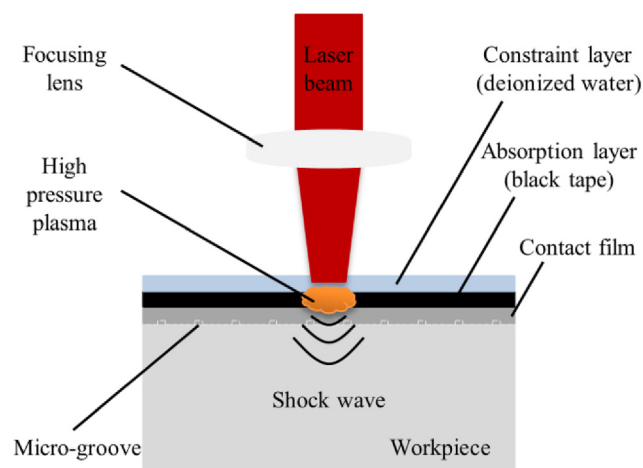


Fig. 1 – Schematic diagram of laser shock imprinting (LSI).

bulges on the workpiece surface, which in shape are complementary to the shape of micro-grooves in contact film. Under the action of the laser shock wave, the rapid spring-back of the high-strength contact film is the key to avoid large depth depression on the workpiece surface, and at the same time, due to the limitation of contact film, the outside of the laser spot zone will not form a flange. As the thickness of contact film is only a few hundred microns, the laser shock wave can still bring about strengthening effects to the workpiece. Importantly, the plastic rheological behavior of the workpiece surface material occurring by the introduction of contact film and its micro-grooves is noteworthy.

Numerical simulation is a high-efficiency and low-cost way to study laser shock technology. In 1999, Braisted et al. [16] first used ABAQUS finite element analysis software to create 2D models to numerically simulate LSP of Ti-6Al-4V alloy and 35CD4 steel. Results from both simulations and experiments were compared to prove the feasibility of numerical simulations. Ding et al. [17] created a 3D model using the same software and analyzed the effect of shock wave pressure magnitude and duration, laser spot diameter and impact number on residual stress field in 35CD4 steel. Li et al. [18] simulated residual stress and energy distribution when TC4 titanium alloy blades were subjected to laser shock at different power densities. Simulation and experimental results were compared to verify the accuracy of finite element model. Zhang et al. [19] simulated a two-sided laser shock on a thin-walled titanium alloy and analyzed the propagation of stress waves as well as their attenuation. Sun et al. [20] simulated LSP of Ti-6Al-4V alloy to analyze the dynamic response during LSP and the residual stress field after LSP. Li et al. [21] adopted flat-top laser beam and Gaussian laser beam to simulate LSP of TC4 titanium alloy as a way to study the effect of spatial energy distribution on residual stresses. Kumar et al. [22] designed an experiment-based LSP simulation model to analyze the effects of different laser parameters (spot diameter, spot overlapping ratio and power density, etc.) on residual stress distribution and surface deformation in Ti-6Al-4V alloy. Wang et al. [23] adopted a simulation strategy of continuous explicit dynamic impact to analyze stress wave propagation process during single laser shock and the effect of different process parameters (e.g. power density, impact number and spot overlapping ratio) on residual stress and plastic strain of TC4 titanium alloy under multiple laser shocks. The above reports indicate that numerical simulation is valuable in understanding residual stress distribution, energy distribution, stress wave propagation and surface plastic deformation, etc. during LSP. With the advancement in computer simulation technology, simulation of LSP has become an integral part of research on the performance of aero-engine blades.

In view of the LSI technology to induce the blade surface material to occur plastic rheological behavior is a short and complex process, the conventional experimental instruments cannot observe this phenomenon. However, the finite element simulation can be clearly observed blade surface material dynamic response process. Therefore, in this paper ABAQUS simulation software is used to study the plastic rheological behavior of LSI aero-engine blade surface material while obtaining the characteristics of the residual stress

distribution and micro-plastic deformation on blade surface, so as to obtain the excellent parameters of the aero-engine blade surface morphology control at a lower cost and provide a new method of the aero-engine blade surface strengthening.

2. Numerical simulation

2.1. Finite element model

In the first step, the simulators of contact film and blade were drawn by Solid Works 3D drawing software. Shape, dimension and arrangement of micro-grooves in contact film are shown in Fig. 2. The number of micro-grooves shown in the schematic is not the actual number. The number of micro-grooves depends on the dimension of contact film (thickness: 0.20 mm). The length of the micro-grooves is 8 mm (this length dimension is not absolute and is determined by the size of the laser shock zone), the width is 0.10 mm, and the depth is 0.02 mm; the spacing between adjacent micro-grooves is 0.40 mm.

In the next step, the simulators of contact film and blade were imported into ABAQUS finite element software as parts for splitting, cutting and dividing the suitable mesh. Mesh division is an important part of finite element simulation as the density of the mesh determines the accuracy and computational efficiency of the final simulation results. Denser the mesh division, more accurate will be the calculated results. However, the time required to solve will increase accordingly, which leads to a decrease in computational efficiency. For this simulation, mesh division was carried out by combining sparsely and densely for contact film and blade parts, considering avoidance of contact penetration due to contact problems in the simulation, and keeping the mesh dimension of contact film parts larger than that of blade parts. This is elaborated below:

- (I) The contact film part is to have micro-grooves, thus the mesh type considered was C3D10 M (10-node modified

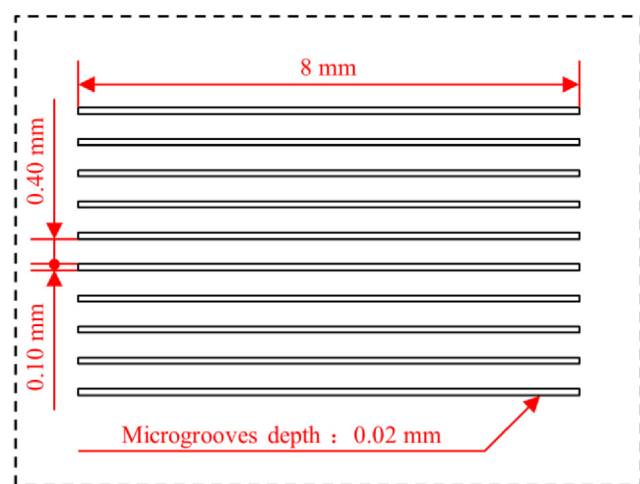


Fig. 2 – Schematic diagram of shape, dimension and arrangement of micro-grooves in contact film.

quadratic tetrahedron element). The mesh seed dimension of the micro-grooves was taken with the dimensions 0.05 mm along the length, 0.05 mm across the width, and 0.02 mm into as the depth, while the rest of the seed dimension of the part was controlled between 0.10 and 0.30 mm. The total number of elements for the contact film parts used in single spot (single impact and multiple impacts) was 240082; the total number of elements for 33%, 50% and 67% overlapping ratios in multi-spot overlapping impacts were 235129, 222931 and 234350, respectively.

- (II) The blade part is the key division object and the mesh type considered was C3D8R (8-node linear brick reduced integration element). The impact zone on blade part requires refined mesh and the transition to the non-impact zone in gradually thickened (mesh seed dimension of the non-associated impact zone was controlled between 0.10 and 2.50 mm). Surface meshing of blade part is critical to obtain accurately the plastic rheological behavior of blade surface. Depending on the shape and dimension of micro-grooves in contact film as well as their specific arrangement, the mesh divided in the X-axis direction in the laser shock zone needs to be finer than that in the Y-axis direction, so as to obtain the exact surface morphology. Considering the depth influence factor of laser shock wave, the mesh density in the Z-axis direction of its impact zone was taken to be between those of the X-axis and Y-axis. In summary, the mesh seed dimension was controlled as 0.01 mm in the X-axis direction, 0.25 mm in the Y-axis direction, and 0.10 mm in the Z-axis direction, and the total number of elements of blade part was 2445379.

In the final step, the contact film part was assembled over the blade part, such that the contact between the two parts was conformal. The finite element model so constructed is shown in Fig. 3. The length of blade body is 130 mm, its width is 45 mm, and its thickness is between 0 and 2 mm (not shown in the figure).

2.2. Material constitutive model

During the laser shock, the material undergoes dynamic plastic deformation at ultra-high strain rates ($\sim 10^7 \text{ s}^{-1}$) in response to laser-induced shock waves [24,25]. Johnson and Cook [26] conducted a wide range of strain rate torsion experiments, static tension experiments, dynamic Hopkinson compression bar tension experiments and Hopkinson compression bar experiments at high temperatures. They proposed the Johnson-Cook (JC) constitutive model for material flow stress. The model is the most widely used material constitutive model based on simulating laser shock processes. The model considers strain effect, strain rate effect and temperature effect, etc., and thus can accurately represent dynamic yield stress and material hardening effect to plastic deformation brought about by the effect. Moreover, in many studies [18,19,21,22], it has been confirmed that the JC model is suitable for laser shock, which is an ultra-high strain rate impact process. The expression of JC model is given below.

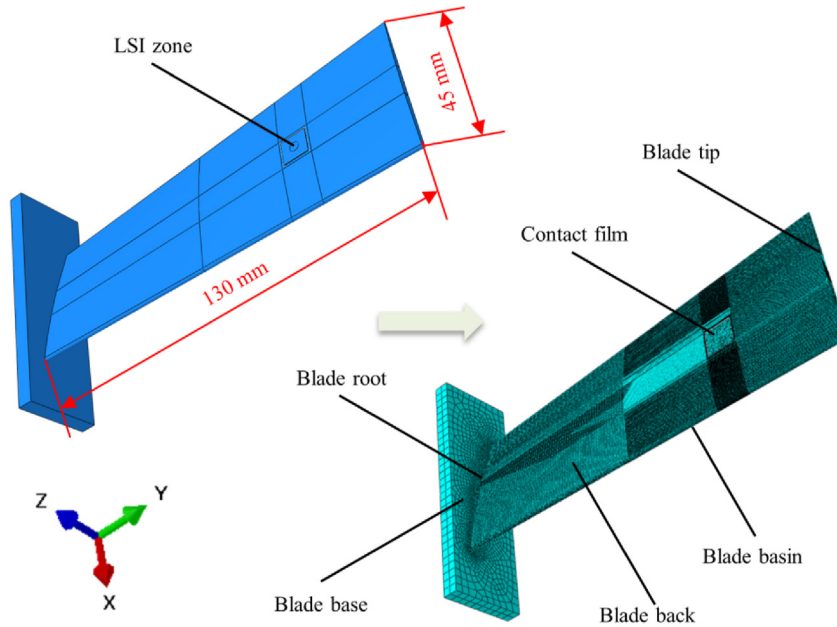


Fig. 3 – Finite element model diagram.

$$\sigma = (A + B\epsilon^n) \left(1 + C \ln \frac{\dot{\epsilon}}{\dot{\epsilon}_0} \right) [1 - (T^*)^m] \quad (1)$$

$$T^* = (t - t_0) / (t_m - t_0) \quad (2)$$

where σ is the equivalent stress, A is the initial yield stress, B is the strain-hardening modulus, ϵ is the equivalent plastic strain, n is the work-hardening index, C is the strain rate strengthening coefficient, $\dot{\epsilon}$ is the equivalent plastic strain rate, $\dot{\epsilon}_0$ is the reference plastic strain rate, m is the thermal softening coefficient, T^* is the dimensionless temperature, t is the material temperature, t_0 is the room temperature and t_m is the melting point temperature.

Absorption and constraint layers carry away most of the heat during laser shock. Hence, metal material is less affected by temperature. Therefore, temperature effect can be neglected during laser shock, and the JC model can be simplified as below [27].

$$\sigma = (A + B\epsilon^n) \left(1 + C \ln \frac{\dot{\epsilon}}{\dot{\epsilon}_0} \right) \quad (3)$$

In this simulation work, 65Mn spring steel film was used as the contact film between the absorption layer and the work-piece (blade). 65Mn spring steel has high strength and high hardness, which meets the selection conditions of contact film material. Mechanical properties of materials (i.e. 65Mn spring steel and TC4 titanium alloy) and JC model parameters for the contact film and blade are given in Table 1 (ρ is the density, E is the elastic modulus, and ν is the Poisson's ratio).

2.3. Pressure loading model

Laser shock wave loading is a thermodynamic transformation process, and the shock wave pressure is considered a special spatiotemporal load that has Gaussian distribution. The

spatial distribution of the laser shock wave can be changed by spatial shaping of the laser beam. In finite element simulations, the laser shock wave is usually simplified to a pressure load that varies with time acting on the surface of a target. When the constraint layer is deionized water film, the shock wave pressure pulse duration is typically 2 to 3 times the width of the laser pulse [30]. The laser pulse width used in this simulation work was 15 ns. Since the shock wave pressure loading occurs in a very short duration of time, according to Braisted et al. [16], the Gaussian curve can be replaced by a triangular slope curve. The triangular slope curve adopted in this simulation work is shown in Fig. 4. The shock wave pressure reaches its amplitude at 1 pulse width (15 ns) and completes loading at 3 pulse widths (45 ns). In order to make the blade surface (curved structure) acquire uniform residual stress distribution, the spatial distribution of the laser shock wave pressure was treated as a uniform load in the spot impact field.

When the peak pressure of the laser shock wave exceeds the Hugoniot elastic limit (HEL) of a material, the material will undergo permanent plastic deformation, resulting in a beneficial compressive residual stress [16]. The peak pressure of the laser shock wave can be estimated by the physical model proposed by Fabbro et al. [31,32]. The model estimates the peak pressure P of the shock wave in terms of the parameters of laser device output, which are related as below.

$$P = 0.01 \sqrt{\frac{\alpha}{2\alpha + 3}} \sqrt{\frac{2Z_1 Z_2}{Z_1 + Z_2}} \sqrt{\frac{4E}{\pi d^2 \tau}} \quad (4)$$

where α is the coefficient of internal energy conversion of heat (usually take 0.1 to 0.2), Z_1 and Z_2 are the shock wave impedance of the target material, respectively and the constraint layer (Z_{TC4} is $2.75 \times 10^6 \text{ g/cm}^2 \cdot \text{s}$ for TC4 titanium alloy and Z_{Water} is $1.65 \times 10^5 \text{ g/cm}^2 \cdot \text{s}$ when deionized water is taken as

Table 1 – Mechanical properties of materials and JC model parameters [28,29].

Material	ρ (kg/m ³)	E (GPa)	ν	A (MPa)	B (MPa)	n	C	$\dot{\epsilon}_0$ (s ⁻¹)
65Mn	7810	200	0.288	980	2000	0.83	0.0026	1
TC4	4510	110	0.34	1098	1092	0.93	0.014	1

the constraint layer [33]), E is the laser pulse energy, d is the spot diameter (in this simulation work, d is 3 mm), and τ is the laser pulse width.

In this simulation work, the loading zone of the laser shock wave pressure is a circular spot zone (single spot impact) with a diameter of 3 mm (which has been determined on the upper surface of contact film part), as shown in Fig. 3 (LSI zone in Fig.). The same applies for multi-spot overlapping mode impacts (consisting of several spots overlapping each other), where the zone to be impacted, is divided in advance on the upper surface of contact film part. The implementation of the overlapping impact path is accomplished through the Step module and the Load module in ABAQUS, where the same loads are applied at different analysis steps, but the loads are applied in different zones, within the zone of each individual circular spot, and the loads are applied one after another in accordance with the overlapping paths of the spots.

2.4. Analytical solution strategy

ABAQUS is a feature-rich engineering finite element software capable of solving complex nonlinear problems. Dynamic loading by laser shock is a typical nonlinear dynamics problem. The numerical simulation process of LSP can be divided into two parts: dynamic response and static spring-back. The ABAQUS/Explicit analysis module is typically used to simulate short, transient dynamic events and is particularly well suited for simulating high-speed impact problems. Therefore, the ABAQUS/Explicit module was adopted to simulate the dynamic response process of the workpiece under the action of shock waves. In order to obtain a stable residual stress field, the dynamic stress and plastic deformation results obtained from the solution of the ABAQUS/Explicit module were set as

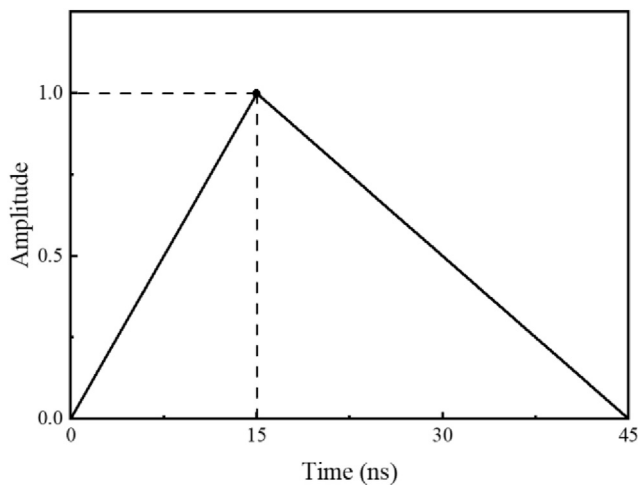


Fig. 4 – Amplitude curve of laser shock wave pressure loading with time.

the initial state and were imported into the ABAQUS/Standard analysis module, and then followed by spring-back analysis.

In this simulation work (taking single spot single impact as an example), in addition to the initial analysis step, there were 4 analysis steps. The dynamic response process was completed by 3 dynamic, explicit analysis steps (the purpose is to accurately capture the evolutionary trends at each stage of the dynamic response process) and the static spring-back process by 1 static, general analysis step. The solution time of Step-1 was set to 50 ns, which was slightly larger than the loading time of shock wave pressure (this was the process of laser shock wave pressure loading); the solution time of Step-2 was set to 4950 ns (this was the process of micro-features formation - fluctuation - equilibrium); the solution time of Step-3 was set to 15000 ns (this was the process of dynamic stress and micro-features changing gradually towards stabilization). To obtain a more stable stress-strain field, the solution time for the static, generic analysis step Step-4 was set to 1 s, then the geometric nonlinearity switch was turned on (set Nlgeom to ON).

In the simulation of LSI, the extrusion behavior of contact film and blade under the action of laser shock waves (i.e. the behavior of blade in terms of surface micro-plastic deformation due to bilateral internal material extrusion and lateral extrusion of micro-grooves in contact film) was achieved using interaction module by creating interactions and applying contact properties on contact surface where the extrusion of the two occurred.

The blade is a typical thin-walled structure. In order to avoid the propagation of shock waves to expand the degree of its macroscopic deformation, the full constraint of blade basin was adopted to control occurrence of large deformation. This reduced its influence on the observation of specific surface micro-features. During the simulation process for multiple or overlapping impacts, in order to avoid the failure of subsequent impacts caused by the excessive springing of the highly elastic contact film, the contact film needs to be replaced after each impact, i.e. before the next impact is considered.

2.5. Numerical model validation

In this simulation work, the convergence of the single point LSI model after meshing is studied, where model A is the model described in the previous section, and both model B and model C are comparative models after mesh subdividing. The total number of elements of models A, B and C are 2685461, 4384849 and 9599418, respectively. The comparison results of stress ($S_{11_{max}}$) and strain ($LE_{11_{max}}$) for the models are shown in Fig. 5. The errors of stress are 3.66%, 0.98% and the errors of strain are 3.95%, 1.15% respectively. The errors of stress and strain are within reasonable limits, so the calculation results of the numerical model in this simulation work have convergence.

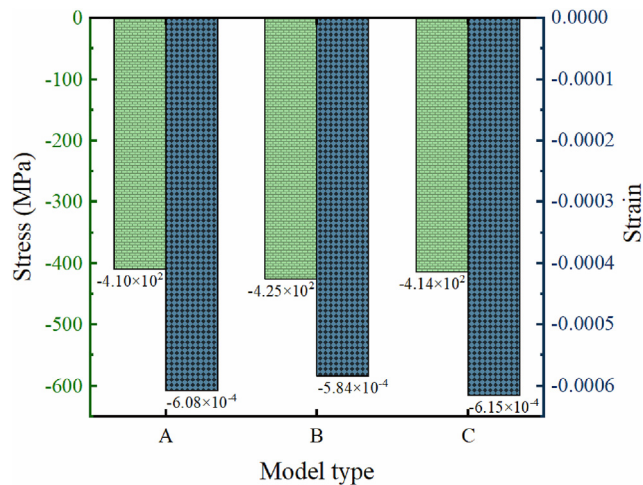


Fig. 5 – Comparison results of numerical simulation.

Meanwhile, the dynamic response process of laser shock (shown in Fig. 6) is an effective means to reflect the accuracy of the model and results. During the LSI process, the laser shock wave propagates to the blade surface after contact film action, and its energy is transferred to the inside of blade material for transformation. As shown in Fig. 6 (a), the total energy of the model is always maintained near 0 mJ, indicating that the model as a whole is in a state of energy balance and the calculation results are more reliable; the kinetic energy of the model increases rapidly under the action of shock wave, and it gradually decays after reaching the peak value. It then enters a stable state after a short period of fluctuation. The plastic dissipation energy increases rapidly within the first 100 ns and then reaches the peak value, after which it remains unchanged. The evolution of dynamic stress and displacement at specific point on blade surface is shown in Fig. 6 (b), the change in dynamic stress and displacement occur within the first 8000 ns. The changes are especially noticeable within the first 5000 ns, and subsequently there are minor fluctuations.

Dynamic deformation behavior of blade surface micro-feature is an important part of the dynamic response process in LSI. The forming height of blade surface micro-feature is defined as the vertical displacement between the apex point and the nadir point of the micro-feature. As shown in Fig. 6 (c), the forming interval of the micro-feature on blade surface occurs within the first 1000 ns. Under the loading and buffering mode of the laser shock wave, the forming height of the micro-feature reaches the first peak value. In view of the spring-back effect of the high-strength contact film, the forming height of the micro-feature decreases and then increases rapidly to reach the second peak value. With the weakening of contact film spring-back effect, the forming height of the micro-feature on blade surface fluctuates and then gradually equilibrates, finally becoming stable after 5000 ns. The change in contact pressure and velocity at the apex point and the nadir point of the micro-feature on blade surface are shown in Fig. 6 (d). After the laser shock wave propagates inside contact film for a period of time, the contact pressure appears on the contact surface between the contact

film and the blade. When the contact pressure reaches the condition for plastic deformation of metal surface, the forming process of the micro-feature on blade surface begins, and the velocity response occurs successively at the nadir point (25 ns) and the apex point (45 ns) of the micro-feature. However, the spring-back of contact film will cause the contact pressure between the contact film and the blade to disappear briefly and then reappear and disappear again. When the apex point and nadir point velocities of the micro-feature remain consistent, it indicates that the micro-feature has formed, which is consistent with the evolution of the micro-feature's forming height in Fig. 6 (c).

The dynamic response results of the above LSI model show that the dynamic analysis step of 20000 ns is sufficient. Thus, adding a static analysis step by 1 s will make the final simulation results more stable and reliable.

In summary, the modeling, parameter settings and calculated results in this simulation work are reliable.

3. Results and discussions

Ballard [34] pointed out that the impact was most effective when the peak shock wave pressure was between 2.0 and 2.5 times Hugoniot elastic limit of material (σ_{HEL}). Hugoniot elastic limit of TC4 titanium alloy is 2.8 GPa [35], and therefore the optimum shock wave peak pressure range is 5.6–7 GPa. In this simulation work, the peak pressure (P) of the laser shock wave (in the case of non-variable) was considered to be 6 GPa, the laser spot diameter (d) was 3 mm, and the laser pulse width (τ) was 15 ns.

Residual stresses induced by LSI on blade surface are differentiated in different directions, due to the directional arrangement of micro-grooves in contact film and the curved structure of blade. As shown in Fig. 7 (a), (b) and (c) (these figures show the results under the task coordinate system CSYS-1, which is the task coordinate system established at the center point of the corresponding spot on blade surface), under the peak pressure of 6 GPa, the maximum compressive residual stress in the X-axis direction is about -410 MPa, the maximum compressive residual stress in the Y-axis direction is about -270 MPa, and the maximum compressive residual stress in the Z-axis direction is about -171 MPa. Their magnitudes are in the order: $S11_{max} > S22_{max} > S33_{max}$. From the stress distribution in different directions, the distribution of residual stress S11 in the X-axis direction is closer to the result that residual stress distribution of blade under laser shock is influenced by arrangement of micro-grooves in contact film. So, S11 (σ_x) was chosen as the stress data in the present simulation work.

The residual stress and micro-plastic deformation of blade surface have different characteristics under the paths of different positions due to the unique shape and arrangement of micro-grooves in contact film. The path selection under single spot impact is shown in Fig. 8. Path 1 is parallel to X-axis and extends outwards with the spot center as the origin, which is the path on the direct contact zone between the blade surface and the contact film, that is, the path on the non-bulge zone of blade surface (in other words, where the ridges of micro-grooves are in contact with the blade surface; dark

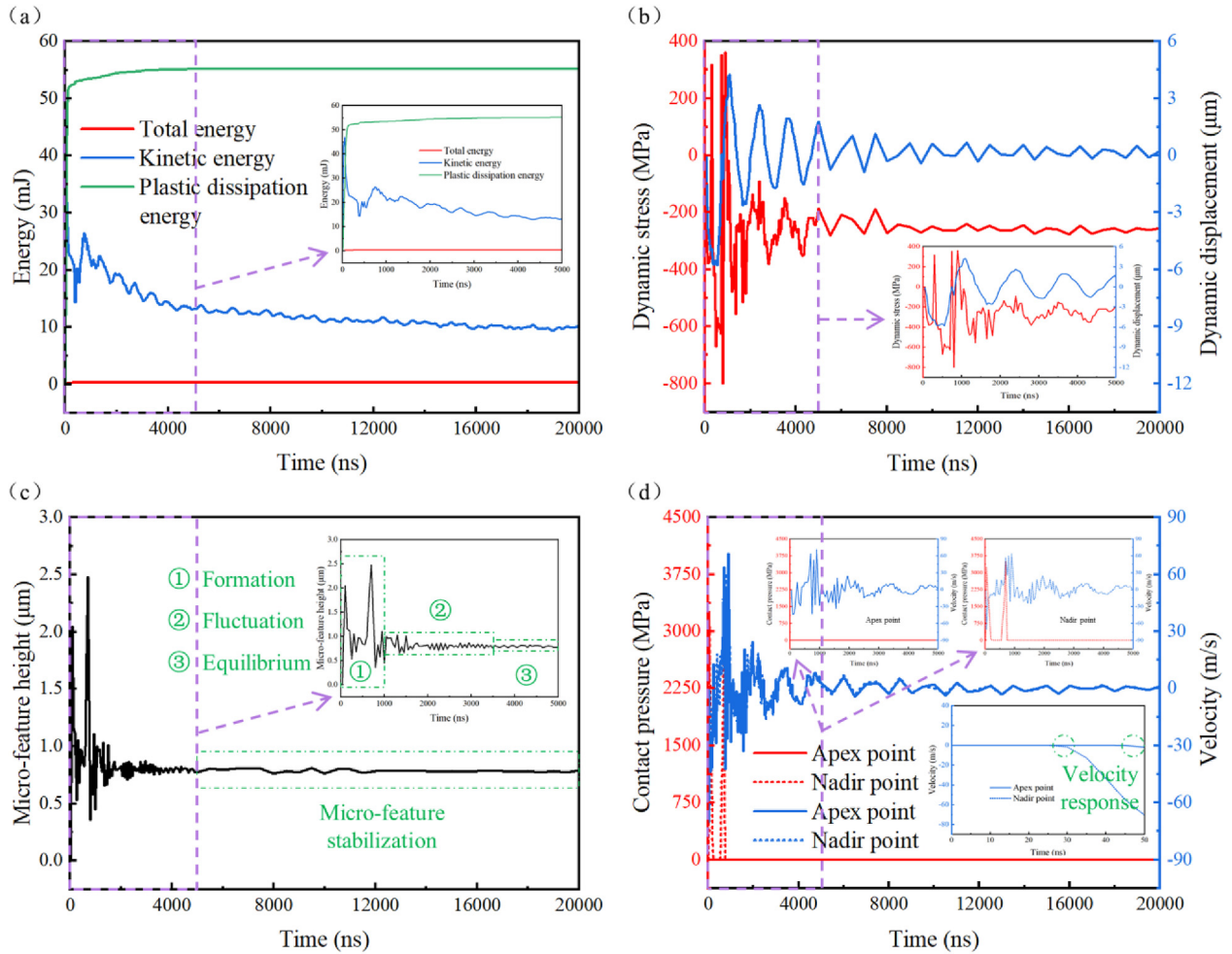


Fig. 6 – Dynamic change of the LSI numerical model: (a) model energy change; (b) dynamic stress and displacement evolution at specific point on blade surface; (c) micro-feature height evolution on blade surface; (d) contact pressure and velocity changes of micro-feature apex and nadir point on blade surface.

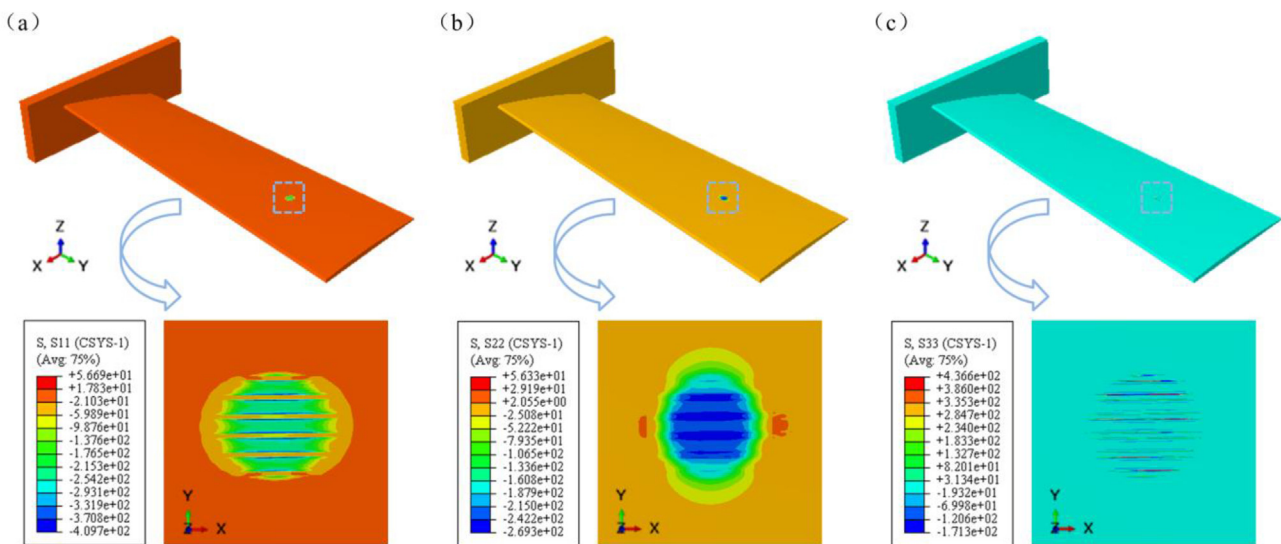


Fig. 7 – Cloud diagram of residual stress distribution on blade in different directions (unit: MPa): (a) residual stress S11 (σ_x) cloud diagram; (b) residual stress S22 (σ_y) cloud diagram; (c) residual stress S33 (σ_z) cloud diagram.

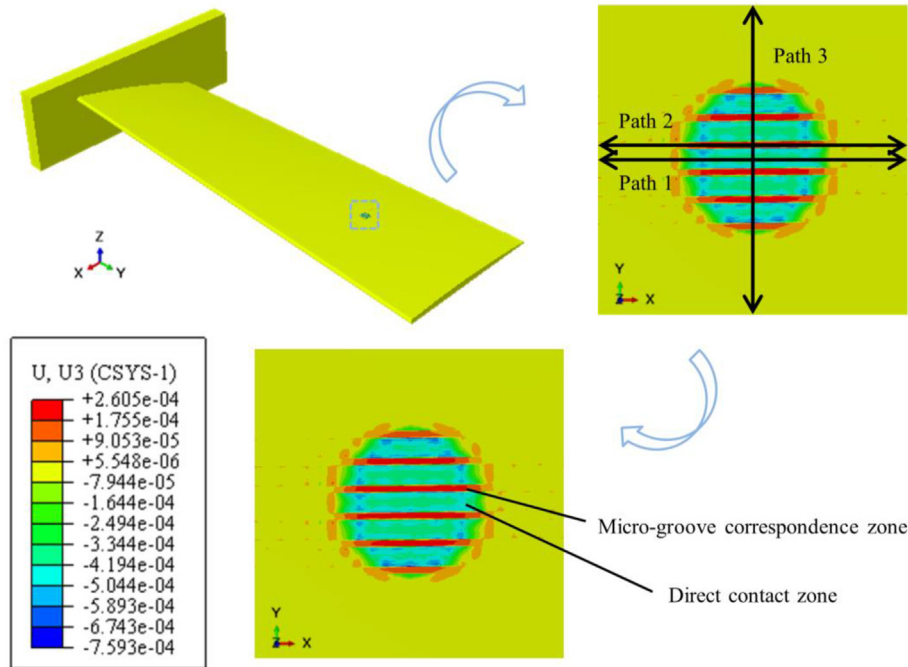


Fig. 8 – Path distribution on blade surface.

green zones inside the spot in Fig. 8). Path 2 is parallel to Path 1 and is the path on the zone where the blade surface corresponds to micro-grooves in contact film, that is, the path on the bulge zone of blade surface (in other words, where the micro-grooves between the ridges are over the blade surface; red zones inside the spot in Fig. 8). Path 3 is parallel to Y-axis (i.e. perpendicular to Path 1 and Path 2) and extends outwards with the spot center as the origin, which is the path over the interlacing arrangement of the zone where the blade surface is in direct contact with the contact film and the zone where the blade surface corresponds to the micro-groove in contact

film, that is, the path on the zone where the non-bulges and bulges on blade surface are interlaced.

Fig. 9 shows the cloud diagram of the effect of LSI on the residual stress and micro-plastic deformation on the surface of the TC4 titanium alloy blade. As shown in Fig. 9 (a), the spot action zone on blade surface is affected by shock wave, and the zone corresponding to the micro-grooves inside the spot (i.e. red zones inside the spot in Fig. 8) is subjected to plastic deformation by extrusion, thus generating compressive residual stresses, which are beneficial for the blade performance. But the compressive residual stresses formed in these

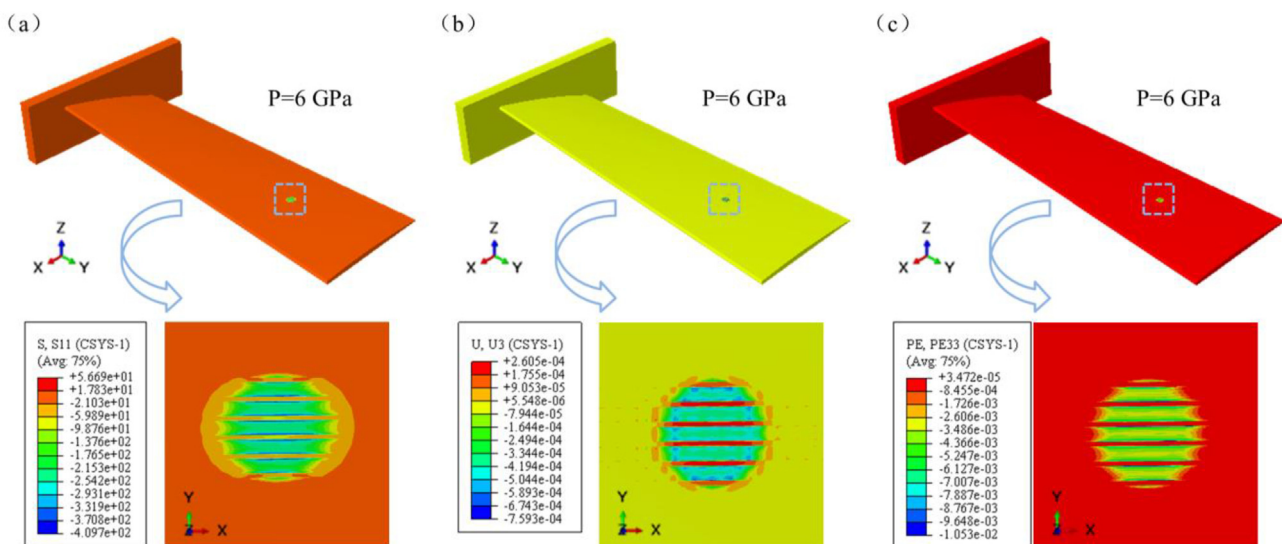


Fig. 9 – Cloud diagram of 6 GPa single spot after single laser shock: (a) residual stress distribution cloud diagram (unit: MPa); (b) surface morphology change cloud diagram (unit: mm); (c) plastic strain distribution cloud diagram.

zones are lower than those in the zone of direct contact between the contact film and the blade (i.e. dark green zones inside the spot in Fig. 8). As shown in Fig. 9 (b), under the reasonable guidance of micro-grooves in contact film, the blade surface forms micro-bulges that complement the micro-grooves morphology, while the non-bulges still show a downward depression similar to that in conventional LSP. As

shown in Fig. 9 (c), the micro-bulge zones on blade surface are not directly affected by the contact pressure between the contact film and the blade, rather they are formed by the extrusion of the material on both sides, so their plastic strain is relatively lower, basically for zero. The non-bulge zones appear to have larger plastic strain because they are directly affected by the planishing action of contact film.

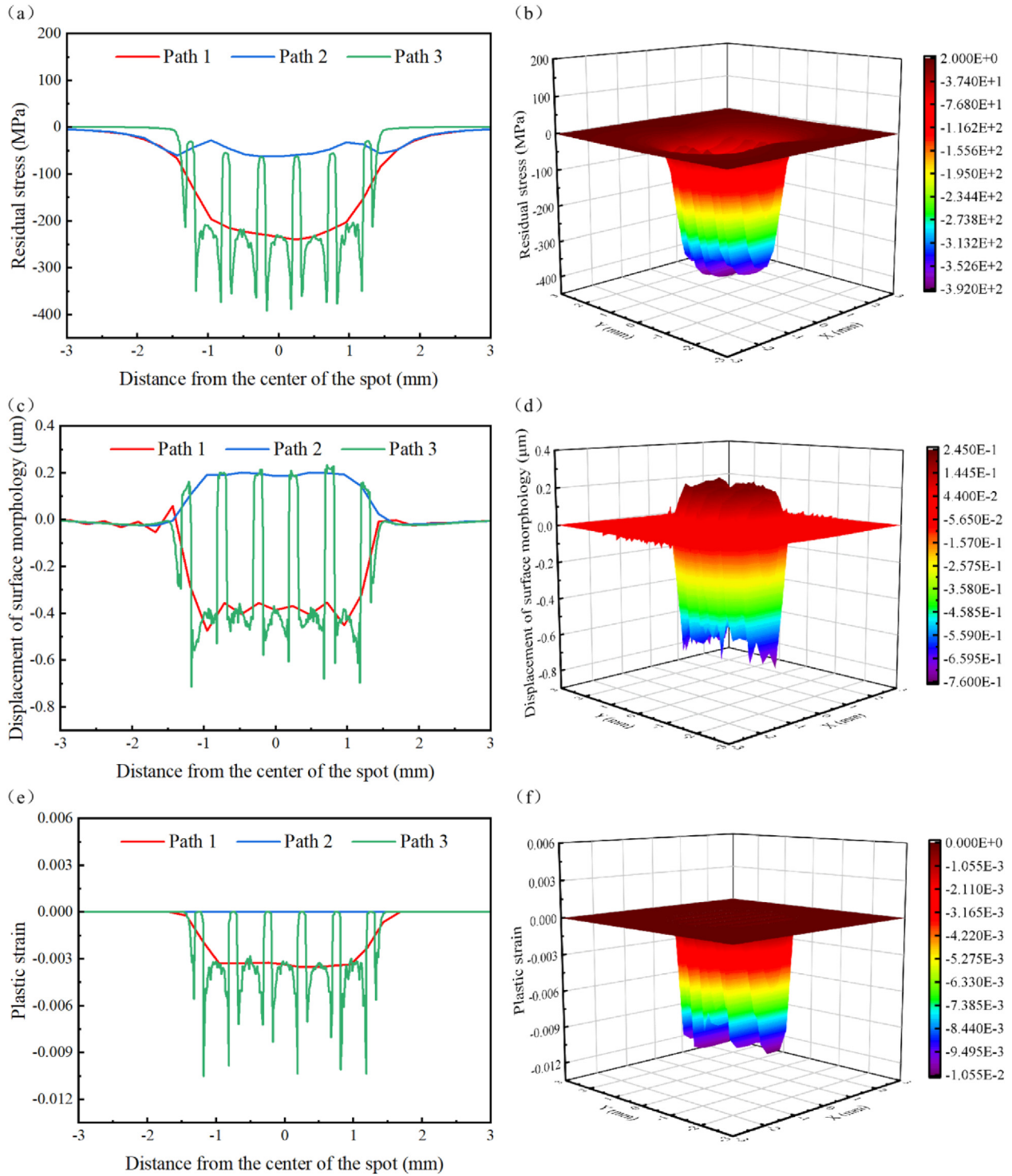


Fig. 10 – Characteristic curves along different paths and 3D surface diagrams: (a) residual stress distribution curve; (b) 3D surface diagram of residual stress distribution; (c) surface morphology change curve; (d) 3D surface diagram of surface morphology change; (e) plastic strain distribution curve; (f) 3D surface diagram of plastic strain distribution.

Fig. 10 shows the residual stress and micro-plastic deformation curves for different paths and their overall 3D surface diagrams. The results presented for Path 1 and Path 2 correspond to the results for the non-bulge and bulge zones of blade surface along Path 3. The residual stress distribution, surface morphology change and plastic strain distribution along Path 3 are closely related to the shape and arrangement of micro-grooves in contact film.

The residual stress distribution is shown in Fig. 1 (a) and (b). The blade surface by the shock wave generates a pit zone, and the stresses in this zone are compressive. The bulge zones are not directly planished by the contact film, and so the compressive residual stresses are small. The bulge zones on both edges of the spot are affected by the spot edges, and the stresses appear to tense upwards, so their compressive stresses are lower than that of the bulge zones in the spot center. The stresses at multiple bulge zones within the pit zone are between -70 and -30 MPa. Therefore, the stress difference between the bulge zones at the edges and the bulge zones at the center of the pit zone makes the stress distribution of multiple bulges appear downwards concave as a whole. The non-bulge zones are directly planished by the contact film, so the compressive stresses generated are higher than those in the bulge zones. The main reason for the formation of compressive residual stress is that the blade surface is affected by micro-grooves in contact film, and plastic deformation occurs due to the extrusion action. Therefore, the compressive residual stresses generated in the bulge edge zones are significantly higher than that in the bulge and non-bulge zones of blade surface, and the maximum compressive residual stress is about -392 MPa.

The surface morphology change is shown in Fig. 10 (c) and (d). Due to spatial and temporal distribution of the laser shock wave, the blade surface will form a pit zone corresponding to the laser spot dimension. The action of contact film and its micro-grooves makes the blade surface undergo plastic deformation because of the bilateral internal material extrusion and extrusion at the side of micro-grooves. Blade material that is in direct contact with the contact film deforms plastically downwards, thus squeezing the material out in the surrounding zones, causing upward plastic deformation of the material in the zones corresponding to the micro-grooves and

forming micro-bulge morphology complementary to the shape of the micro-grooves, which extends upwards from the bottom of the pit. The height of the micro-bulge is the vertical displacement from the bulge nadir point to the apex point, which is about $0.94 \mu\text{m}$. The apex of the formed bulge is about $0.20 \mu\text{m}$ above the non-impacted zone of blade surface. The overall morphology of the multiple bulges is relatively uniform, while the deformation of the edge zones affected by extrusion is slightly uneven, with a maximum plastic deformation displacement of $0.76 \mu\text{m}$ in the downward direction.

The plastic strain distribution is shown in Fig. 10 (e) and (f). The plastic strain in the bulge zones of blade surface is zero, as these zones are not directly subjected to the contact pressure of contact film. Almost no plastic strain is generated, which is consistent with the non-impacted zones of blade surface. The overall plastic strain is stable and is approximately -0.0035 in the non-bulge zones. However, in the zones where the blade surface material undergoes extrusion, the plastic strains are larger, and the maximum plastic strain is approximately -0.0105 .

Fig. 11 shows the relationship between residual stress distribution and micro-plastic deformation on blade surface along Path 3. The trends of residual stress distribution, surface morphology change, and plastic strain distribution are influenced by the arrangement of micro-grooves in contact film, and their trends are highly consistent. Under the action of the laser shock wave, affected by micro-grooves in contact film, the blade undergoes plastic deformation due to bilateral internal material extrusion and lateral extrusion of micro-grooves in contact film, making its surface have bulge and non-bulge zones. The plastic deformation causes compressive residual stresses beneficial to blade performance and creates a uniform stress difference between the bulge and non-bulge zones. The stress-strain values are higher in the micro-bulge edge zones that are subjected to significant extrusion. Different deformations and different contact conditions in different zones lead to different stress distributions at different plastic strain levels, but the residual stress distribution, surface morphology change, and plastic strain distribution are in a more uniform state from the overall view of the spot zone.

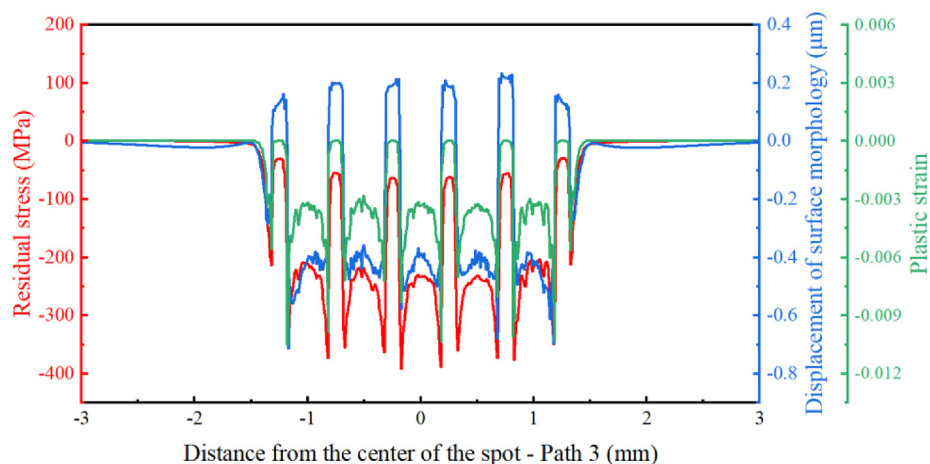


Fig. 11 – Relation between residual stress distribution and micro-plastic deformation characteristics along Path 3.

The process parameters of laser shock have a significant influence on the impact effect. Simulations in this work focus on the effects of peak pressure, impact number and spot overlapping ratio on residual stresses and micro-plastic deformation. For the micro-plastic deformation of single spot impact, the main focus is on the surface morphology change of the impact zone on blade surface.

3.1. Effect of peak pressure on surface residual stress and micro-plastic deformation

The peak pressure of the shock wave is one of the important factors affecting the effect of LSI. The peak pressures considered for the simulation were 4 GPa, 5 GPa, 6 GPa, 7 GPa and 8 GPa.

Fig. 12 (a) shows the residual stress distribution curves at different peak pressures (Path 3). As the peak pressure increases, the compressive residual stress generated on blade surface also increases. For the different peak pressures, the maximum compressive residual stresses obtained were about -76 MPa, -217 MPa, -392 MPa, -565 MPa and -746 MPa, respectively. The stress difference between the bulge zones and the non-bulge zones increases with the peak pressure. The stress difference generated by the action of 4 GPa peak pressure is not significant, indicating that the stress difference can only occur under high-pressure loading. The stress difference between the bulging edge and the non-bulge zones decreases with the increase in peak pressure, because the peak pressure increases cause plastic deformation between the bulging edge and the non-bulge zones to be close, reducing the stress difference between them. However, the larger stress difference between the bulge and non-bulge zones still makes the residual stress distribution in the whole spot action zone uneven with increasing peak pressure.

Fig. 12 (b) shows the surface morphology change curves at different peak pressures (Path 3). As the peak pressure increases, the height of the bulge and the depth of the non-bulge on blade surface also increase. For the different peak pressures, the maximum heights of micro-bulge apices obtained were 0.06 μm , 0.12 μm , 0.23 μm , 0.39 μm and 0.53 μm , respectively; while the maximum depths of pit sinking were 0.14 μm , 0.40 μm , 0.71 μm , 1.09 μm and 1.56 μm , respectively.

With increasing depths, the height difference between them became more significant. The apex height of the micro-bulge and the sinking depth of the pit together determine the surface roughness of blade, and the surface roughness at high-peak pressure is greater and more likely to destroy the surface integrity of blade.

Under the premise of obtaining higher compressive residual stress, the selection of peak pressure not only needs to pay attention to the overall molding height of the micro-bulge but also to consider the surface sinking caused by the high peak pressure. For example, upon 4 GPa impact, the surface morphology appears uniform, but the compressive residual stress generated is too small. Upon 8 GPa impact, the residual stress generated is very large, but the gap between its overall bulge and depression is too large. Considering the relationship between the height of the bulge within the pit and the depth of sinking of the pit, combined with the magnitude of compressive residual stress, the 6 GPa peak pressure is appropriate in all aspects and is within the optimal shock wave peak pressure range.

3.2. Effect of impact number on surface residual stress and micro-plastic deformation

Excessive peak pressure will cause ablation on blade surface, and also the problems of excessive deformation and layer cleavage will occur [33], which are detrimental to the surface integrity of blade. However, a single impact usually does not provide the desired effect, and so it usually requires multiple impacts of small energy to obtain a greater compressive residual stress and the depth of its affecting layer. The impact numbers considered for the simulation were 1, 2, 3, 4 and 5 impacts.

Fig. 13 (a) shows the residual stress distribution curves at different impact numbers (Path 3). As the impact number increases, the compressive residual stress generated on blade surface also increases. For the different impact numbers, the maximum compressive residual stresses obtained were about -392 MPa, -544 MPa, -643 MPa, -704 MPa and -744 MPa, respectively. The stress difference between the bulge zones and the non-bulge zones increases with the impact number. But the increase in compressive residual stress shows

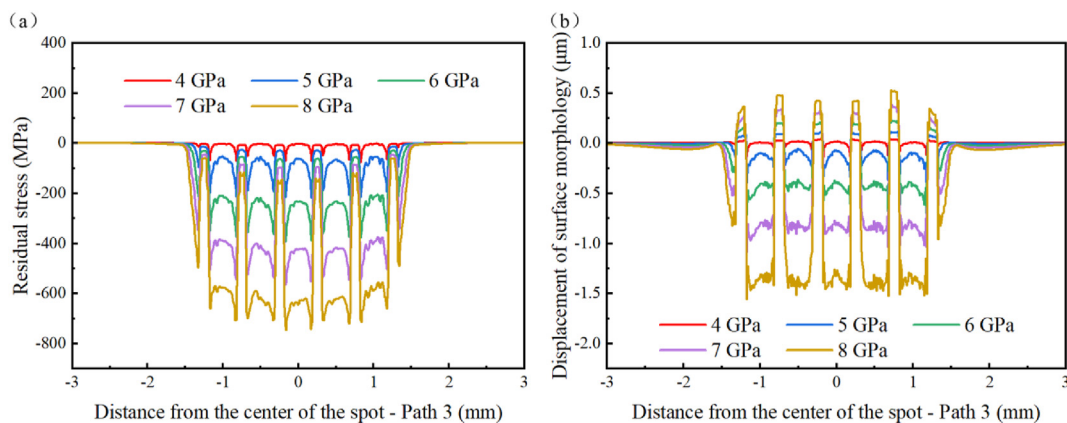


Fig. 12 – Characteristic curves at different peak pressures: (a) residual stress distribution curve; (b) surface morphology change curve.

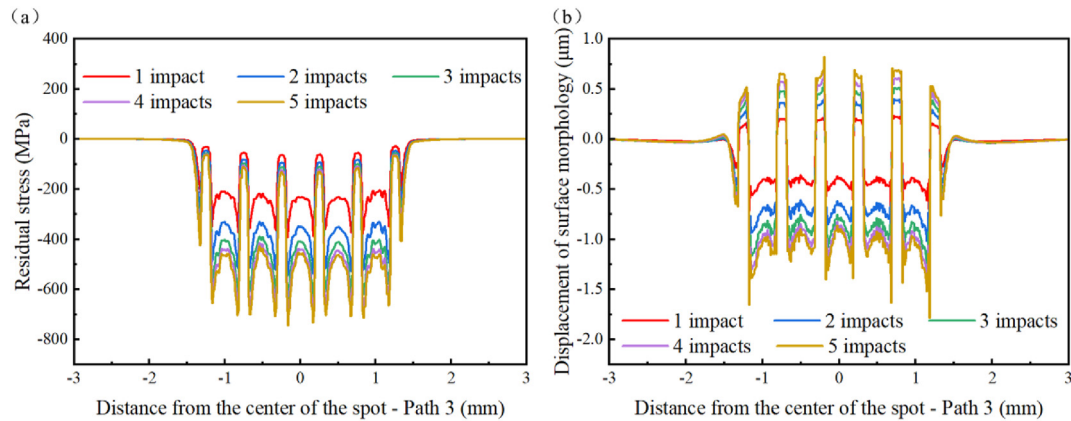


Fig. 13 – Characteristic curves at different impact numbers: (a) residual stress distribution curve; (b) surface morphology change curve.

a multiply decreasing trend. 2 impacts compared to 1 impact, the maximum compressive residual stress increases by -152 MPa, an increase of 38.78%. 3 impacts compared to 2 impacts, an increase of 18.20%. Over 3 impacts, the compressive residual stress gradually saturates and the increase is not significant, while the maximum compressive residual stress increases by 9.49% for 4 impacts compared to 3 impacts, and only by 5.68% for 5 impacts compared to 4 impacts. Multiple laser shocks cause process hardening of blade surface, increasing both strength and hardness at the same time, resulting in a reduction in plastic deformation and consequently reducing the magnitude of compressive residual stress.

Fig. 13 (b) shows the surface morphology change curves at different impact numbers (Path 3). As the impact number increases, the height of the bulge and the depth of the non-bulge on blade surface also increase. For the different impact numbers, the maximum heights of micro-bulge apices obtained were $0.23\ \mu\text{m}$, $0.40\ \mu\text{m}$, $0.56\ \mu\text{m}$, $0.69\ \mu\text{m}$ and $0.82\ \mu\text{m}$, respectively; while the maximum depths of pit sinking were $0.71\ \mu\text{m}$, $1.13\ \mu\text{m}$, $1.43\ \mu\text{m}$, $1.63\ \mu\text{m}$ and $1.78\ \mu\text{m}$, respectively. From 1 impact to 2 impacts is the most significant for the increased height of the bulge apex and the sinking in depth of the pit. 3 impacts and above, the displacement change in the non-bulge zones reaches saturation. High impact number makes plastic deformation fluctuate significantly, so the bulge heights and their edge depths become very uneven between the different bulges, and the surface roughness substantially increases. This would cause destructive damage, and would adversely affect the overall integrity of blade surface. Combined with the compressive residual stress distribution and surface morphology change induced by multiple impacts, the number of laser shocks selected was 3 impacts or less.

3.3. Effect of spot overlapping ratio on surface residual stress and micro-plastic deformation

Irradiation area of laser beam is limited, and for a workpiece that requires a large area of laser shock, it must rely on spot overlapping for impact coverage of the workpiece. Too small overlapping ratio does not completely cover the zone to be

impacted. Theoretically, the circular laser spot overlapping ratio should be at least 29.29% to ensure full coverage of the impact zone. The spot overlapping ratios considered for the simulations were 33%, 50% and 67%, respectively. The spot overlapping ratio is calculated as:

$$\eta = \left(1 - \frac{S}{2R}\right) \times 100\% \quad (5)$$

where η is the spot overlapping ratio, S is the distance between adjacent spots, and R is the laser spot radius. Table 2 shows the parameters used in Eq. (5) for different overlapping ratios. Fig. 14 shows a schematic diagram of spot overlapping. Yellow arrow line shows the spot overlapping path.

The overlapping of spots means that different impact numbers will be generated in different zones. Therefore, to study the spot overlapping effect on residual stresses and micro-plastic deformation (at different spot overlapping ratios), the selected paths within the impact zone will be different. As shown in Fig. 15 (under 9 spots of overlapping), for the convenience of distinguishing the paths of single spots, the paths selected on blade surface under spot overlapping are named as Path A, Path B and Path C*. Different from the path selection of a single spot, the path parallel to the X-axis direction no longer distinguishes the zones of direct contact between the blade and the contact film or the zones where the blade corresponds to the micro-grooves. Path A is parallel to X-axis, and the path extends outwards with the spot overlapping center as the origin; Path B is parallel to Y-axis, and the path extends outwards with the spot overlapping center as the origin; Path C* is parallel to Path B, which is the path on the spot multi-overlap zone. At 33% spot overlapping ratio,

Table 2 – Eq. (5) parameters at different spot overlapping ratios.

η	S (mm)	R (mm)
33%	2.0	1.5
50%	1.5	1.5
67%	1.0	1.5

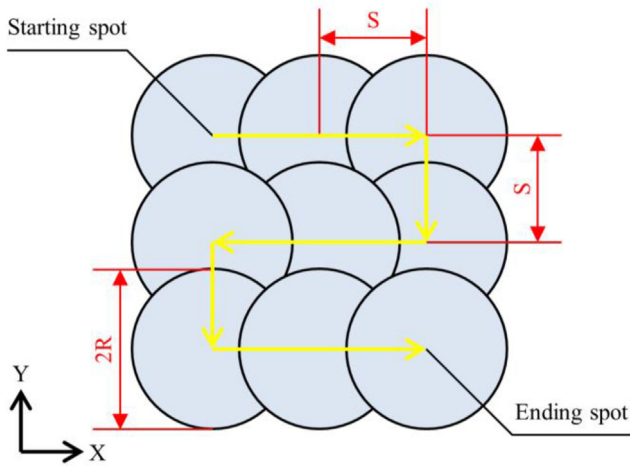


Fig. 14 – Schematic diagram of spot overlapping (33%).

there is a zone of at most 2 impacts along Path A and Path B, while Path C1 has a zone of 4 impacts. At 50% spot overlapping ratio, the situation in the zone where Path A, Path B and Path C2 appear with multiple impacts is consistent with that at 33% spot overlapping ratio, but Path A and Path B are affected because of their location at the boundary of the spot. At 67% spot overlapping ratio, the zone with up to 9 impacts exists along Path A and Path B, while Path C3 also has a zone with high impact number.

Fig. 16 shows the cloud diagram of residual stress distribution, surface morphology change and plastic strain distribution at different spot overlapping ratios. It can be seen from the residual stress cloud diagram Fig. 16 (a), (d) and (g) that for the different overlapping ratios, the maximum compressive residual stresses obtained were about -610 MPa, -768 MPa and -892 MPa, respectively. The increase in compressive residual stress is positively correlated with the spot overlapping. As the overlapping ratio increases, the stress difference

between the overlapping and non-overlapping zones becomes more significant, while the zone with multiple impacts on blade has a greater compressive residual stress. The stress at 67% spot overlapping ratio fluctuates most significantly in the surrounding zones. It can be seen from the surface morphology cloud diagram Fig. 16 (b), (e) and (h) that for the different overlapping ratios, the maximum heights of micro-bulge apexes obtained were approximately $0.36 \mu\text{m}$, $0.66 \mu\text{m}$ and $0.84 \mu\text{m}$; while the maximum depths of pit sinking were approximately $1.33 \mu\text{m}$, $1.97 \mu\text{m}$ and $2.41 \mu\text{m}$, respectively. The impact at 50% spot overlapping ratio has the greatest influence on the surface morphology change at the outer edge of the spot overlapping. It can be seen from the plastic strain cloud diagram Fig. 16 (c), (f) and (i) that for the different overlapping ratios, the maximum plastic strains obtained were 0.0155 , 0.0199 and 0.0236 , respectively. The plastic strain in the impact zone of blade surface is minimal and almost zero in all micro-bulge zones.

Fig. 17 (a) shows the residual stress distribution curves (Path C*) at different spot overlapping ratios. As the spot overlapping ratio increases, the compressive residual stress generated on blade surface also increases. For the different spot overlapping ratios, the maximum compressive residual stresses obtained were about -539 MPa, -665 MPa and -826 MPa, respectively. The zone of maximum compressive residual stress generation is where the spots are most heavily overlapped, which is subjected to the highest impact numbers. From 33% to 50% and then to 67% of the spot overlapping ratios, the increases in the maximum compressive residual stresses are 23.38% and 24.21% , respectively, with only 0.83% increase. The reason is that at 67% of the spot overlapping although exists higher overlapping zone, high impact number will cause the compressive residual stress to gradually reach a saturation state.

Fig. 17 (b) shows the surface morphology change curves (Path C*) at different spot overlapping ratios. As the spot overlapping ratio increases, the height of the bulge and the depth of the non-bulge on blade surface also increase. For the

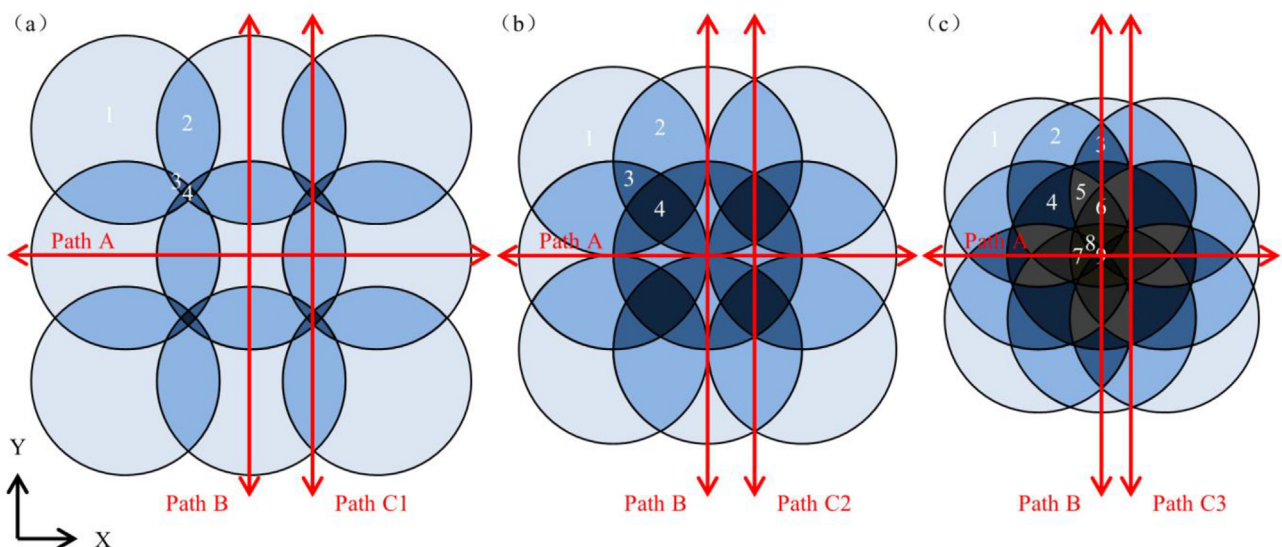


Fig. 15 – Path selection at different spot overlapping ratios: (a) 33%; (b) 50%; (c) 67%.

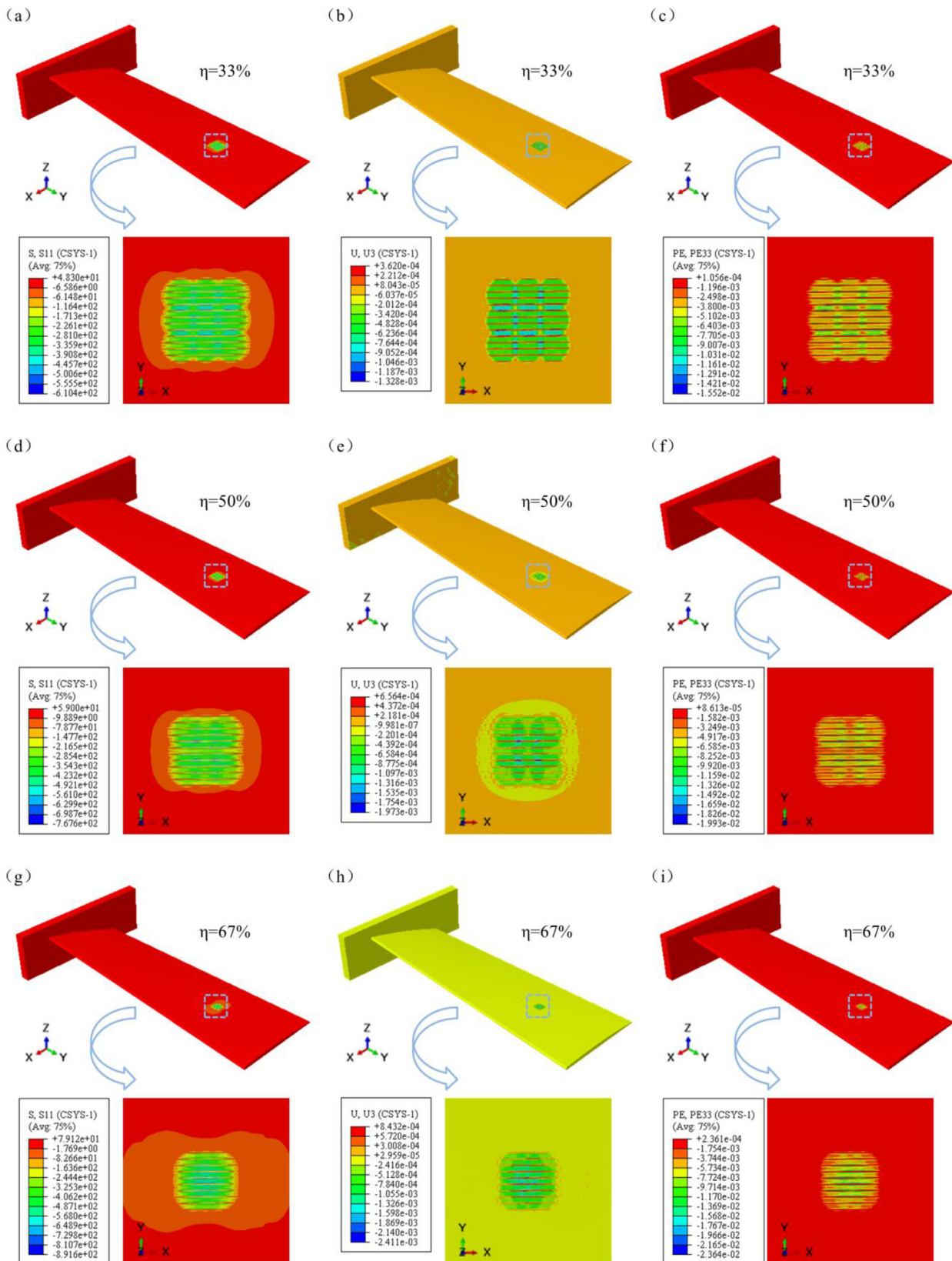


Fig. 16 – Cloud diagram at different spot overlapping ratios: (a), (d), (g) residual stress distribution cloud diagram (unit: MPa); (b), (e), (h) surface morphology change cloud diagram (unit: mm); (c), (f), (i) plastic strain distribution cloud diagram.

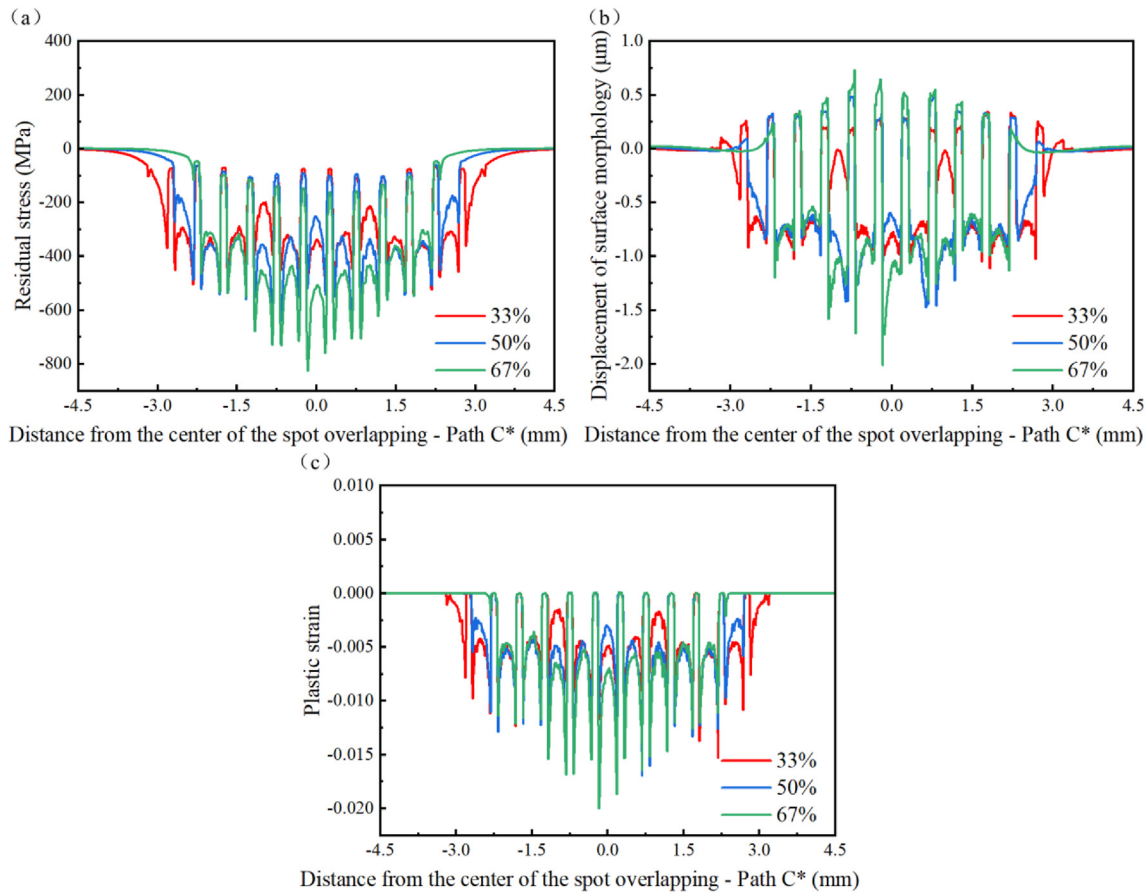


Fig. 17 – Characteristic curves at different spot overlapping ratios: (a) residual stress distribution curve; (b) surface morphology change curve; (c) plastic strain distribution curve.

different spot overlapping ratios, the maximum heights of micro-bulge apices obtained were $0.35\ \mu\text{m}$, $0.51\ \mu\text{m}$ and $0.73\ \mu\text{m}$, respectively; while the maximum depths of pit sinking were $1.11\ \mu\text{m}$, $1.47\ \mu\text{m}$ and $2.01\ \mu\text{m}$, respectively. At 33% spot overlapping ratio, the overall bulge height is more uniform. At 50% spot overlapping ratio, the overall bulge height presents a small part of unevenness. At 67% spot overlapping ratio, the overall bulge height is particularly poor uniformity, and the degree of plastic deformation in some zones is very significant, affects adversely the morphology of the entire overlapping zones of blade.

Fig. 17 (c) shows the plastic strain distribution curves (Path C*) at different spot overlapping ratios. As the spot overlapping ratio increases, the plastic strain on blade surface also increases. For the different spot overlapping ratios, the maximum plastic strains obtained were 0.0153, 0.0170 and 0.0200, respectively. The plastic strain in each bulge zone is minimum and almost zero; the plastic strain in the bulging edge is much larger than that in the non-bulge zone, and the difference between them becomes larger in the multi-overlap zone.

For aero-engine blades that are high-precision, complex curved thin-walled types of parts, surface integrity requirements are extremely high, and so it is not appropriate to use high overlapping ratios (>50%) of spot overlapping to impact. The overlapping ratio of 33% can control the

micro-plastic deformation on blade surface in a smaller range while ensuring high amplitude compressive residual stress. Also, in this case, the micro-bulges on blade surface are more uniform, as well as the area of the impact zone is wider, which is conducive to the improvement of the efficiency of laser shock. The characteristics of residual stresses and micro-plastic deformations generated by the LSI technology depend on the arrangement of micro-grooves and their morphological characteristics, so Path B and Path C* better reflect the impact morphology of the spot overlapping zones.

Fig. 18 shows 33% spot overlapping ratio effect on the residual stress distribution and surface morphology change along different paths. In Path B, the conventional impact zones are interlaced with the secondary overlapping zones; in Path C1, the secondary overlapping zones are interlaced with the quadruple overlapping zones, but the overall overlapping is dominated by the spot secondary overlapping.

The residual stress distribution is shown in Fig. 18 (a) and (c). In Path B, the compressive residual stresses in multiple bulge zones are very uniform and are not affected by the spot overlapping. However, there is a significant increase in the compressive residual stresses in the non-bulge zones in the secondary overlapping zones compared to the non-overlapping zones. In Path C1, the compressive residual stresses in the bulge zones (in the secondary overlapping

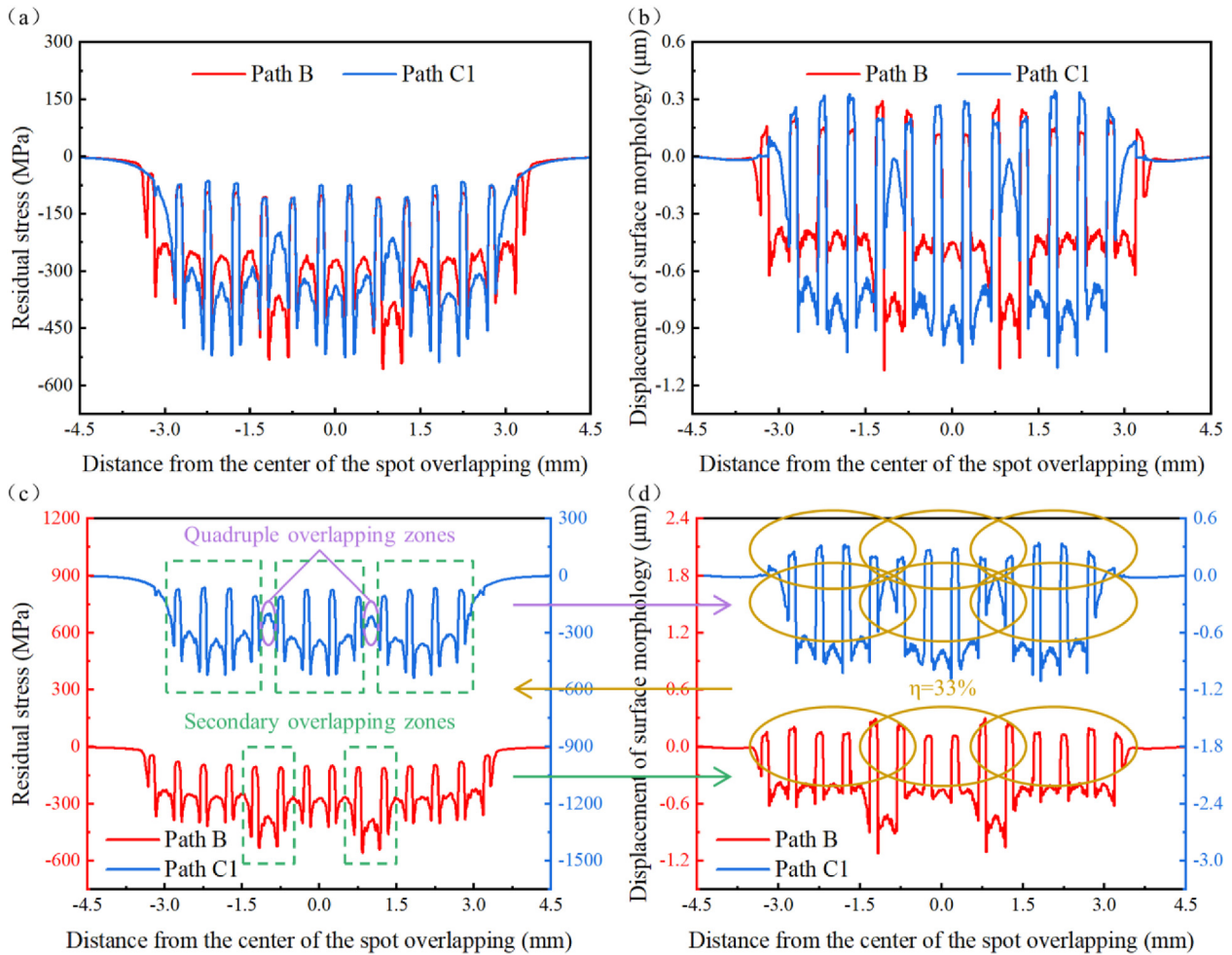


Fig. 18 – Characteristic curves of Path B and Path C1 at 33% spot overlapping ratio: (a), (c) residual stress distribution curve; (b), (d) surface morphology change curve.

zones) next to the quadruple overlapping zones are larger compared to the other bulge zones. The range of the quadruple overlapping zones is small and is affected by the spot boundary, so that the non-bulge zones have a tendency to be convex upward, thus reducing the compressive residual stresses. Due to the spot boundary effect, there is a difference between Path B and Path C1 for the compressive residual stresses in both secondary overlapping zones.

The surface morphology change is shown in Fig. 18 (b) and (d). In Path B, the maximum heights of the bulge apexes in the secondary overlapping zones are greater than those in the non-overlapping zones, so are the maximum depths of pit sinking. In Path C1, the heights of the bulges around the quadruple overlapping zones are lower than the others, and the quadruple overlapping zones are located at the boundary of multiple spots, which do not show a greater depth of sinking, but rather a reverse bulge trend. The sinking depths of the secondary overlapping zones in Path B are more consistent with the sinking depths of each spot center in Path C1, but the heights of the bulges are still slightly different. Generally, the overall morphology in the zone of the multiple spots is more uniform, and the roughness of blade surface is effectively controlled.

4. Conclusions

ABAQUS finite element models were used for TC4 titanium alloy blades to conduct numerical simulation studies of laser shock imprinting (LSI) in order to reveal the characteristics of residual stress distribution and micro-plastic deformation on blade surface. The simulation was conducted at different peak pressures, impact numbers and spot overlapping ratios. Following are the conclusions drawn from the simulation work:

- (1) LSI made the blade surface subject to the double action of laser shock wave and the micro-grooves in contact film, made realize accurate control of the micro-plastic deformation (uniform micro-bulge morphology) on blade surface. This greatly improved the complex and uncontrollable micro-plastic deformation (depression and flange interlacing morphology) caused by conventional LSP due to spot overlapping.
- (2) LSI induced controlled micro-plastic deformation on blade surface. Its plastic rheological behavior made the distribution of stress-strain on blade surface change by

the influence of surface morphology, which produced significant stress-strain differences at the bulging edge, non-bulge and bulge zones.

- (3) When the blade was subjected to LSI, the increase in the impact number did not decrease the stress difference between the bulging edge and the non-bulge zones as much as by the increase in the peak pressure. Increase in the impact number maintained a certain value of stress difference between the bulging edge, non-bulge and bulge zones. The impact number showed more effect on the surface morphology change in the impact zone of blade compared to the peak pressure.
- (4) The overlapping of the laser spot not only covered a larger area of the zone to be impacted but also promoted beneficial compressive residual stresses in the zone. The spot overlapping ratio of 33% effectively controlled the surface micro-morphology induced by laser shock waves, which produced uniform bulge morphology in the zone of multiple spots acting on blade surface.

Declaration of competing interest

The authors declare that they have no known competing financial interests or personal relationships that could have appeared to influence the work reported in this paper.

Acknowledgments

The authors are grateful for the support provided by Key Research and Development Project Zhejiang Province (2021C04022).

REFERENCES

- [1] Lin JW, Zhang JH, Zhang GC, Ni GJ, Bi FR. Aero-engine blade fatigue analysis based on nonlinear continuum damage model using neural networks. *Chin J Mech Eng* 2012;25(2):338–45.
- [2] Poursaeidi E, Bakhtiari H. Fatigue crack growth simulation in a first stage of compressor blade. *Eng Fail Anal* 2014;45:314–25.
- [3] Nie XF, Li YH, He WF, Luo SH, Zhou LC. Research progress and prospects of laser shock peening technology in aero-engine components. *J Mech Eng* 2021;57(16):293–305.
- [4] Kulyk M, Koveshnikov M, Petruk Y, Petruk B, Yakushenko O. Thermocyclic fatigue and destruction of high pressure turbine blades in their critical sections. *Transport Res Procedia* 2022;63:2812–9.
- [5] Zheng J. Research on key manufacturing technology of aero-engine blade. *Plant Maint Eng* 2019;(24):89–90.
- [6] Zhang LJ, Xue XY, Chang H. Deformation of titanium alloy materials for China aircraft. *Mater Chin* 2012;31(8):40–6.
- [7] Wang FS, Wang AL, Chen YJ, Zhou S. High temperature mechanical properties of aeronautical TC4 titanium alloy. *Hot Work Technol* 2017;46(10):86–89+93.
- [8] Singh P, Pungotra H, Kalsi NS. On the characteristics of titanium alloys for the aircraft applications. *Mater Today Proc* 2017;4(8):8971–82.
- [9] Wu JF, Che ZG, Zou SK, Cao ZW, Sun RJ. Surface integrity of TA19 notched simulated blades with laser shock peening and its effect on fatigue strength. *J Mater Eng Perform* 2020;29(prepublish):1–11.
- [10] Qin R, Zhang ZF, Hu ZY, Du ZY, Xiang XW, Wen GR, et al. On-line evaluation and monitoring technology for material surface integrity in laser shock peening – a review. *J Mater Process Technol* 2023;313:117851.
- [11] Peyre P, Fabbro R. Laser shock processing: a review of the physics and applications. *Opt Quant Electron* 1995;27(12):1213–29.
- [12] Sundar R, Ganesh P, Ram KG, Ragvendra G, Pant BK, Vivekanand K, et al. Laser shock peening and its applications: a review. *Lasers Manuf Mater Process* 2019;6(4):424–63.
- [13] Bartsch TM. High cycle fatigue (HCF) science and technology program 2002 annual report. Dayton, Oh: Univ Technol Corp; 2003.
- [14] Wang MY, Kononov S, Dai FZ, Chen XZ. Influence of process parameters on laser shock processing effect of aero-engine blades. *J Surf Invest X-ray Synchrotron Neutron Tech* 2022;16(6):1208–20.
- [15] Maharjan N, Chan SY, Ramesh T, Nai PG, Ardi DT. Fatigue performance of laser shock peened Ti6Al4V and Al6061-T6 alloys. *Fatigue Fract Eng Mater Struct* 2020;44(3):733–47.
- [16] Braisted W, Brockman R. Finite element simulation of laser shock peening. *Int J Fatigue* 1999;21(7):719–24.
- [17] Ding K, Ye L. Three-dimensional dynamic finite element analysis of multiple laser shock peening processes. *Surf Eng* 2003;19(5):351–8.
- [18] Li PY, Huang SK, Xu HF, Li YX, Hou XL, Wang QD, et al. Numerical simulation and experiments of titanium alloy engine blades based on laser shock processing. *Aerosp Sci Technol* 2015;40(Jan):164–70.
- [19] Zhang XQ, Li H, Duan SW, Yu XL, Feng JY, Wang B, et al. Modeling of residual stress field induced in Ti–6Al–4V alloy plate by two sided laser shock processing. *Surf Coat Technol* 2015;280:163–73.
- [20] Sun RJ, Li LH, Zhu Y, Zhang LX, Guo W, Peng P, et al. Dynamic response and residual stress fields of Ti6Al4V alloy under shock wave induced by laser shock peening. *Model Simul Mater Sci Eng* 2017;25(6):065016.
- [21] Li X, He WF, Luo SH, Nie XF, Tian L, Feng XT, et al. Simulation and experimental study on residual stress distribution in titanium alloy treated by laser shock peening with flat-top and Gaussian laser beams. *Materials* 2019;12(8):1343.
- [22] Kumar GR, Rajyalakshmi G. FE simulation for stress distribution and surface deformation in Ti-6Al-4V induced by interaction of multi scale laser shock peening parameters. *Optik* 2020;206(C):164280.
- [23] Wang BH, Cheng L, Ding JL, Cui WB, Wang CK, Li DC. Numerical simulation on laser shock peening of TC4 titanium ally. *J Aerosp Power* 2021;36(5):959–68.
- [24] Zhang YK, Zhou LC, Ren XD, Li Y, Lu JZ. Experiment and finite element analysis on residual stress field in laser shock processing TC4 titanium alloy. *J Jiangsu Univ (Nat Sci Ed)* 2009;30(1):10–13+18.
- [25] Xu G, Luo KY, Dai FZ, Lu JZ. Effects of scanning path and overlapping rate on residual stress of 316L stainless steel blade subjected to massive laser shock peening treatment with square spots. *Appl Surf Sci* 2019;481(C):1053–63.
- [26] Johnson GR, Cook WH. A constitutive model and data for metals subjected to large strains, high strain rates and high temperatures. *Eng Fract Mech* 1983;21:541–8.
- [27] Johnson GR, Cook WH. Fracture characteristics of three metals subjected to various strains, strain rates, temperatures and pressures. *Eng Fract Mech* 1985;21(1):31–48.

-
- [28] Cheng W, Dai FZ, Huang S, Konovalov S, Chen XZ. Surface topography control of TA2 pure titanium in laser shock peening. *Metals* 2022;12(6):1031.
- [29] Sekar KSV, Kumar MP. Finite element simulations of Ti6Al4V titanium alloy machining to assess material model parameters of the Johnson-Cook constitutive equation. *J Braz Soc Mech Sci Eng* 2011;33(2):203–11.
- [30] Berthe L, Fabbro R, Peyre P, Tollier L, Bartnicki E. Shock waves from a water-confined laser-generated plasma. *J Appl Phys* 1998;82(6):2826.
- [31] Fabbro R, Fournier J, Ballard P, Devaux D, Virmont J. Physical study of laser-produced plasma in confined geometry. *J Appl Phys* 1990;68(2):775–84.
- [32] Peyre P, Fabbro R, Merrien P, Lieurade HP. Laser shock processing of aluminium alloys. Application to high cycle fatigue behavior. *Mater Sci Eng, A* 1996;210(1):102–13.
- [33] Yang FH. Research on numerical simulation of TC4 alloy simulated blade by laser shock peening. *Guangdong Univ Technol*; 2019.
- [34] Ballard P. Residual stresses induce by rapid impact application of laser shocking. France: Ecole Poly Tech 1991:20–56.
- [35] Fang YW, Li YH, He WF, Li PY. Effects of laser shock processing with different parameters and ways on residual stresses fields of a TC4 alloy blade. *Mater Sci Eng, A* 2013;559:683–92.